

Observations of ocean surface wave attenuation in sea ice using seafloor cables

Madison M. Smith¹, Jim Thomson², Michael G. Baker³, Robert E. Abbott³,
Jake Davis²

¹Woods Hole Oceanographic Institution, Woods Hole, MA, USA

²Applied Physics Laboratory, University of Washington, Seattle, WA, USA

³Sandia National Laboratories, Albuquerque, NM, USA

Key Points:

- Seafloor fiber optic cables can be used to quantify surface waves in seasonally sea ice-covered oceans
- High spatial-resolution wave observations may be used to study wave attenuation in ice at much finer resolution than previously possible
- The rapid evolution of the location and strength of attenuation serves as proxy for the evolution of ice itself

Corresponding author: Madison M. Smith, madisonmsmith@whoi.edu

Abstract

The attenuation of ocean surface waves during seasonal ice cover is an important control on the evolution of many Arctic coastlines. The spatial and temporal variations in this process has been challenging to resolve with conventional sampling using sparse arrays of moorings or buoys. We demonstrate a novel method for persistent observation of wave-ice interactions using distributed acoustic sensing (DAS) along existing seafloor telecommunications cables. The DAS measurements span a 36 km cross-shore seafloor cable on the Beaufort Shelf from Oliktok Point, Alaska. DAS measurements of strain-rate provide a proxy for seafloor pressure, which we calibrate with wave buoy measurements during the ice-free season (August 2022). We apply this calibration during the ice formation season (November 2021) to obtain unprecedented resolution of variable wave attenuation rates in new, partial ice cover. The location and strength of wave attenuation serve as a proxy for ice coverage and thickness, especially during rapidly-evolving events.

Plain Language Summary

Coasts globally are susceptible to erosion by ocean waves. In the Arctic, sea ice near the coast can serve as protection for much of the year. It is particularly challenging to measure waves and ice in this environment, which is necessary to understand the degree of buffering and project future changes. Typical ways of observing waves (e.g., buoys and underwater moorings) have lower success in coastal ice. We show a new way to observe waves and ice in these coastal regions using cables at the seabed deployed for internet connection. With the use of an instrument called an interrogator, these cables can act like a series of hundreds of wave buoys. This allows us to see that waves are reduced at a variable rate throughout the ice. There are significant opportunities to learn more about the coastal Arctic using this novel technology and method.

1 Introduction

Sea ice attenuates surface wave energy through a variety of scattering and dissipative processes (e.g., Squire, 2019). Wave attenuation rates typically increase with frequency, with magnitude that varies as a function of ice type, coverage, and thickness (Meylan et al., 2018; Kohout et al., 2020; Rogers et al., 2021). Wave attenuation in new ice such as frazil and pancakes is typically dominated by dissipative processes (Kohout & Meylan, 2008) resulting in relatively low wave energy attenuation due to typically low thickness and concentration that is typical (Cheng et al., 2017; Hošeková et al., 2020). Progress in understanding wave attenuation in sea ice has been somewhat hindered by the limitation of observing apparent attenuation between widely-spaced discrete wave measurement locations, such that it is challenging to spatially resolve the evolution of the processes (Thomson, 2022). For example, Hošeková et al. (2020) identify high attenuation rates within 500 m of an ice edge, relative to the attenuation farther within the ice, but lack sufficient data to explain the phenomenon.

Landfast ice typically extends 5-20 km in the cross-shore direction in the coastal Arctic (Mahoney, 2018), and provides sufficient attenuation to buffer the coast from most wave energy (Hošeková et al., 2021). In the Alaskan Arctic, landfast ice is predominantly seasonal (Mahoney et al., 2014), with dramatic transitions at spring break-out and autumn freeze-up. The coastal system is then more exposed to ocean waves and heat in the absence of this ice (Barnhart et al., 2014). Understanding the seasonal transitions of landfast ice and annual exposure to waves is necessary to understand the degree of buffering and to project future changes in inundation and erosion.

Measurements of waves in the coastal Arctic are challenging not only during partially ice-covered seasons, but also during open water periods because of logistical chal-

64 lenges including the remote location and shallow water depths. Distributed acoustic sens-
 65 ing (DAS) of seafloor fiber optic cables is an emerging technology that offers a partic-
 66 ularly appealing method for observing spatial and temporal changes in surface waves in
 67 remote and seasonally ice-covered coastal environments. Seafloor DAS (or ocean-bottom
 68 DAS, OBDAS) has previously been demonstrated to be capable of observing ocean sur-
 69 face waves (Lindsey et al., 2019; Williams et al., 2019), and methods are rapidly evol-
 70 ving for use quantifying a range of other oceanographic and geophysical processes (Baker
 71 & Abbott, 2022; Landrø et al., 2022; Wilcock et al., 2023). Measurements of such high
 72 spatial resolution are generally unprecedented in Polar regions.

73 This work demonstrates the quality and fidelity of DAS for ocean surface wave mea-
 74 surements in both open water and partially ice-covered periods in the coastal Arctic. In
 75 particular, estimates of wave attenuation are both consistent with previously observed
 76 values and reveal new spatial variability. Attenuation observations can serve as an in-
 77 dication of changes in ice extent and thickness during rapidly-evolving events. This can
 78 include ice loss (melting) and formation (freezing), as well as advection of sea ice.

79 2 Methods

80 2.1 DAS observations

81 Observations presented here use DAS records from a cross-shore seafloor transect
 82 on the Beaufort Shelf. Data were recorded on dark fiber in a branch of a telecommuni-
 83 cation cable owned by Quintillion and extending northwards from the landing site at Oli-
 84 tok Point, Alaska, to a maximum of 37.4 km offshore (Figure 1a). The maximum wa-
 85 ter depth along this transect is 19.7 m, and the depth of cable burial is approximately
 86 2 m until 16.1 km along-cable distance, then approximately 4 m beyond that. The fiber
 87 was interrogated using a Silixa iDAS interrogator during one-week periods in Novem-
 88 ber 2021 and August 2022 (Baker & Abbott, 2022). The interrogator measures cable strain-
 89 rate in units of nm/m/s. The cable is spliced at 16.1 km, coincident with the change in
 90 depth of fiber burial. Both the splice and depth-of-burial difference result in a change
 91 in sensitivity at this location.

92 Data was recorded in 15-s chunks at a channel spacing of 2 m (10-m gauge length)
 93 and sample rate of 1000 Hz (1 kHz). Data records were concatenated to 1-hr segments
 94 and downsampled to 40 m and 2 Hz to reduce data volumes for this work, as 2 Hz should
 95 be sufficient to capture any ocean surface gravity wave signals that are observable at the
 96 seafloor over the range of water depths measured. Temporal downsampling was completed
 97 by transforming raw data to the frequency domain with a zero-padded 2N fft with $N =$
 98 3.6×10^6 , which is then convolved with a zero-phase lowpass FIR filter with cutoff fre-
 99 quency of 1 Hz. This is then transformed back to the time domain with every 500th sam-
 100 ple extracted.

101 2.2 Wave buoy measurements

102 A moored SWIFT wave buoy (Thomson, 2012) (Figure 1b) was deployed August
 103 14–September 1 2022 to provide in situ surface wave comparison for the seafloor DAS.
 104 The buoy was deployed at 16.2 km along-cable distance (70.62°N , 150°W ; orange point
 105 in Figure 1a), in approximately 12.6 m water depth. Waves are measured using a com-
 106 bination GPS and IMU receiver with a 12-minute record at the top of each hour follow-
 107 ing the details in Thomson et al. (2018). Horizontal velocity vectors are decomposed into
 108 mean and wave orbital velocity components to infer wave energy spectra (Herbers et al.,
 109 2012). Spectra were processed up to 1 Hz, with bulk parameters of significant wave height
 110 (H_s) and energy-weighted wave period (T_e) calculated over 0.03–0.5 Hz to avoid the noise
 111 common in higher frequencies of observations (Thomson, Lund, et al., 2021). Significant

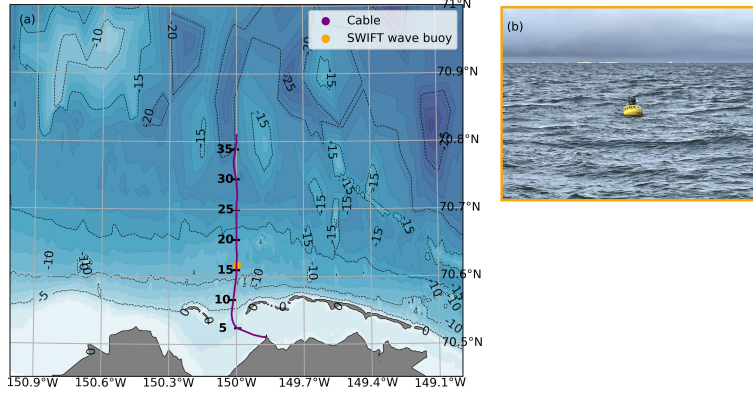


Figure 1. (a) Map of observations near Oliktok Point, Alaska, with the seafloor cable used for DAS measurements in purple and SWIFT wave buoy (August 2022) in orange. Black tick labels show along-cable distance in km. Background contours show bathymetry from NOAA navigation maps (Baker & Abbott, 2022) in meters. (b) Photo of a moored SWIFT wave buoy in open water.

112 wave height is defined as $H_s = 4\sqrt{\int E(f) df}$ and energy-weighted wave period is de-
 113 fined as $T_e = \frac{\int E(f) df}{\int E(f) \cdot f df}$.

114 2.3 Calculation of DAS empirical correction factor

115 The measurement of strain-rate by DAS is used as a proxy for the seafloor pres-
 116 sure. In order to convert it to a spectrum that can be used to approximate wave param-
 117 eters, we derive a frequency-dependent empirical correction factor for each channel (i.e.,
 118 each location along the cable). The correction factor calculation uses all measurements
 119 from the open-water record August 16-21, 2022, when the SWIFT wave buoy was de-
 120 ployed concurrently. The calibration dataset covers a relatively small range of wave heights
 121 (0-0.5 m) and periods (2.5-3.5 s), where waves at similar shelf locations typically range
 122 from around 0-2 m (Thomson et al., 2020) seasonally. In future experiments, calibration
 123 with datasets covering a larger range of likely conditions may result in a more robust cal-
 124 ibration, but such a dataset does not currently exist for this location. Additionally, fiber
 125 strain has been found to be linearly related to the temperature change of the cable (Sidenko
 126 et al., 2022). We expect this to have a small impact on the applicability of August cal-
 127 ibration to the seasonal wave period due to the cable burial depth which should result
 128 in relatively slow temperature response to the variation of seafloor water temperature
 129 likely between -1.8 and 2 °C (Thomson et al., 2020).

130 The empirical correction factor is calculated as a ratio of the power spectral den-
 131 sity (PSD) of strain-rate and wave-driven seafloor pressure. We calculate the PSD of the
 132 raw strain-rate in each hour-long timestep using Welch’s overlapped segment averaging
 133 estimator which uses a Hamming window of length 128 with 50% overlap. The SWIFT
 134 wave spectra from the same hour is identified, and a depth attenuation correction is ap-
 135 plied to infer the expected seafloor pressure. The expected depth-dependent attenuation
 136 of wave energy is e^{2kd} , where d is the water depth and k is wavenumber from the linear
 137 surface gravity wave dispersion relation. Dividing the spectrum of seafloor pressure by
 138 the strain-rate spectrum gives an empirical correction factor (Figure A1). This is repeated
 139 for each timestep, and the empirical correction function is defined as the median of the
 140 correction factor for each timestep (Figure A2).

The process is repeated for all channels outside of the barrier islands (8 km to 35 km along-cable distance). While the location of the wave buoy used for calibration is up to 18 km away from the DAS channels analyzed, we assume here that the calibration dataset is sufficiently long that spatial homogeneity can be assumed. The two most likely violations of the homogeneity assumption would be shoaling and local fetch-limited wind-wave generation. Shoaling is evaluated using the square root of the ratio of the group velocity between the deepest and shallowest sites. The resulting shoaling coefficient is close to unity (~ 1.05) and thus does not cause much change in wave height along the cable. Fetch-limited generation can cause larger changes (up to 50%), but only causes gradual increases with the square root of distance (Thomson & Rogers, 2014).

2.4 Calculation and evaluation of DAS surface wave estimates

To derive corrected surface wave spectra from DAS observations, PSD of strain-rate (calculated using the Welch’s method described in 2.3 above) are multiplied by the channel-specific frequency-dependent empirical correction factor (e.g., Fig. A2) and divided by the depth-attenuation correction (e^{2kd}). Upper spectral cutoffs are subjectively determined for corrected wave spectra at each timestep as an inflection point beyond which the shape does not suggest surface waves and appears to be dominated by noise (Thomson, Lund, et al., 2021). Beyond this cutoff, spectra are fit with the canonical f^{-4} for high-frequencies waves (e.g., Liu, 1989) (Figure A3).

Bulk wave characteristics are calculated from the corrected spectra using standard definitions over the frequency range of 0.03–0.5 Hz. The time series of bulk wave characteristics for the open-water calibration period is shown in Figure 2 (purple lines). Leave-one-out cross-validation is used to evaluate the methodology by estimating the out-of-sample error between bulk parameters derived from corrected DAS spectra and the buoy (orange lines). For all N coincident buoy and DAS observations during the 6-day observation period, a single time-step is excluded and the remaining $N-1$ observations are used to produce a median correction factor. The bulk parameter estimates are then evaluated on the left out test point. This gives RMSE = 0.10 meters and $R^2 = 0.84$ for H_s , and RMSE = 0.65 seconds and $R^2 = 0.52$ for T_e for the channel at 16.2 km closest to the buoy. Error is higher for T_e in part because larger values are more likely than for H_s , as well as that it is more sensitive to the higher frequencies that may not be as well resolved by seafloor DAS.

Wave spectra and bulk parameters can then also be calculated for other periods by applying the channel-specific empirical correction factor, including the November 2021 observation period presented here.

2.5 Wave attenuation rates

Wave attenuation by sea ice as a function of frequency, $\alpha(f)$, is calculated between two points (denoted by subscripts 1 and 2) as

$$\alpha(f) = \frac{1}{\Delta x} \ln \frac{E_1(f)}{E_2(f)} \quad (1)$$

where $E(f)$ is the spectral wave energy as a function of frequency and Δx is the distance between points 1 and 2. A bulk attenuation can also be calculated by using the bulk wave height (H_s) in place of frequency-dependent wave energy. The difference between a height attenuation rate and an energy attenuation rate is simply a factor of 2, because energy E depends on H^2 . Attenuation calculated using wave height is most common and easily comparable with literature values, and the upper frequency cutoff used in the calculation avoids the known rollover at high frequencies in ice associated with noise (Thomson, Hošeková, et al., 2021). For completeness, we also show attenuation values at 0.1 and 0.2 Hz (\times and $+$ in Fig. 3). We calculate the attenuation at 200 m intervals averaged

over a 4 km distance by averaging together attenuation results calculated using all DAS-derived wave observations within each 4 km region. This produces smoother and more realistic attenuation results than from using individual spectra, but still captures the high spatial variability.

3 Results

3.1 Waves in open water, August 2022

Time series of bulk wave parameters during the open water observation period in August 2022 from both observational datasets are shown in Figure 2. The sea state was characterized by wind sea with energy-weighted periods (T_e) of 2.3–3.5 s measured by both the SWIFT wave buoy and the DAS channel closest to the buoy location. Wave heights peaked late on August 17 into early August 18. Peak wave heights of over 0.4 m were measured by the SWIFT wave buoy, while wave heights were somewhat overestimated by DAS at around 0.5 m at August 17 18:00. A gap in the DAS record from August 17 23:00 – August 18 19:00 missed the remainder of the event.

We also compare wave measurements from both methods with bulk wave parameters provided by the European Centre for Medium-Range Weather Forecasts (ECMWF) Reanalysis v5 (ERA5) hindcast product (Hersbach et al., 2020). The waves from this reanalysis have already been shown to be inaccurate during seasonal transitions, when the hindcast lacks the necessary resolution (Hošeková et al., 2021). The native grid resolution of 31 km cannot be expected to capture on-shelf processes, though there is some representation of sub-grid bathymetry as “obstructions” that should be especially important for transformation of longer waves (Bidlot, 2012). Still, the ERA5 products are being used to assess coastal exposure in Alaskan Arctic regions given the dearth of other sufficient data (e.g., Hošeková et al., 2021; Cohn et al., 2022), and thus we include it here for completeness. Waves are significantly overestimated by the hindcast (blue line in Figure 2), with significant wave heights double that observed by the wave buoy during the peak wave event and more than 4x larger during low-wave periods. The measurements from the DAS show significant improvement in capturing wave parameters compared to the hindcast. Throughout a range of wave conditions typical of the open water season, seafloor cable DAS can provide a high-fidelity method for capturing nearshore wave forcing and subsequent coastal wave exposure (e.g., Hošeková et al., 2021).

3.2 Wave attenuation during fall ice advance, November 2021

DAS measurements during the week of November 10, 2021, were coincident with the advance of new landfast ice over the cable near Oliktok Point (Baker & Abbott, 2022). We focus our analysis on distances from 10–25 km along-cable due to signal-to-noise issues outside that range. A spatial cross-section of wave retrievals from November 10, 17:00 (Figure 3) demonstrates characteristics of the spatial patterns of wave evolution in new, autumn sea ice. This is consistent with Sentinel-1A synthetic aperture radar (SAR) imagery from earlier on the same date (November 11, 03:22, Figure 4b) which shows new ice formation both inshore of approximately 18 km along-cable distance and beyond 35 km (outside of the measurement range), with a patch of open water between. ERA5 suggests wind speeds of around 12 m/s in the early hours of November 10, providing sufficient energy for shoreward wave generation in the open water patch. Wave heights and energy-weighted wave periods show spatial variability with distance from offshore to on-shore that is characteristic of wave attenuation in sea ice. Wave heights decrease notably over this distance, peaking at a height of 1.0 m offshore and approaching the lower observable limit (< 0.05 m) near 12 km. Energy-weighted periods are approximately constant around 5 s from 20 km to 25 km along-cable distance, where we begin to see a shift towards higher periods (lower frequencies) with a peak of around 10 s. This increase in mean wave period is associated with spectral down-shifting characteristic of waves in ice

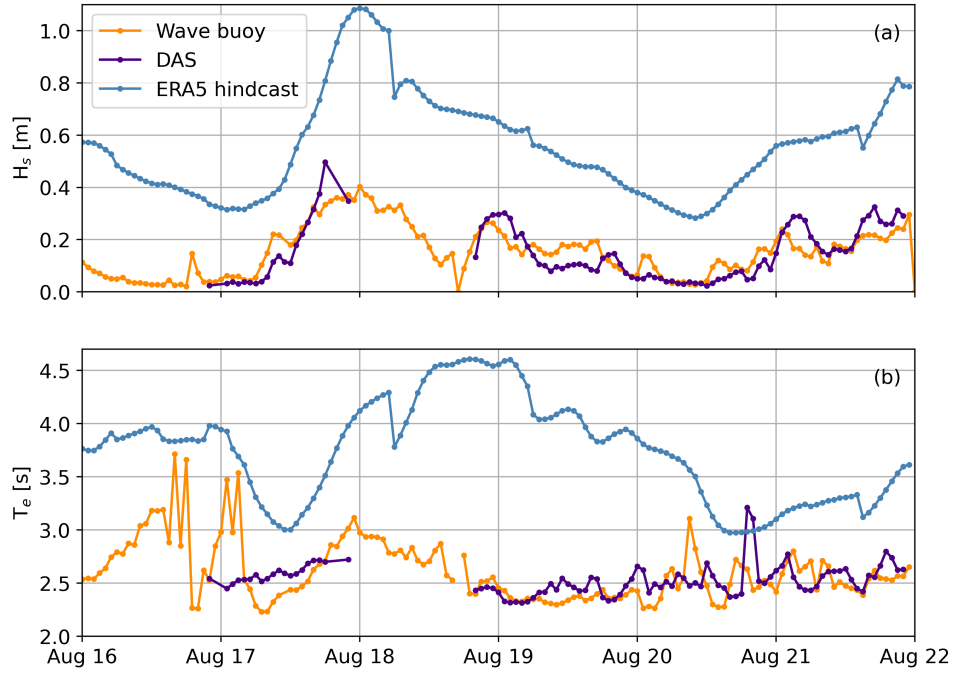


Figure 2. Time series of (a) significant wave height, (b) and energy-weighted wave period as measured by SWIFT wave buoy (orange), seafloor cable DAS (purple; 16.2 km along-cable distance), and estimated by ERA5 hindcast model (blue). Buoy and ERA5 hindcast cover the period from August 16–22, 2022, while DAS observations are available for August 16 22:00 – August 17 22:00 and August 18 20:00 – August 21 22:00.

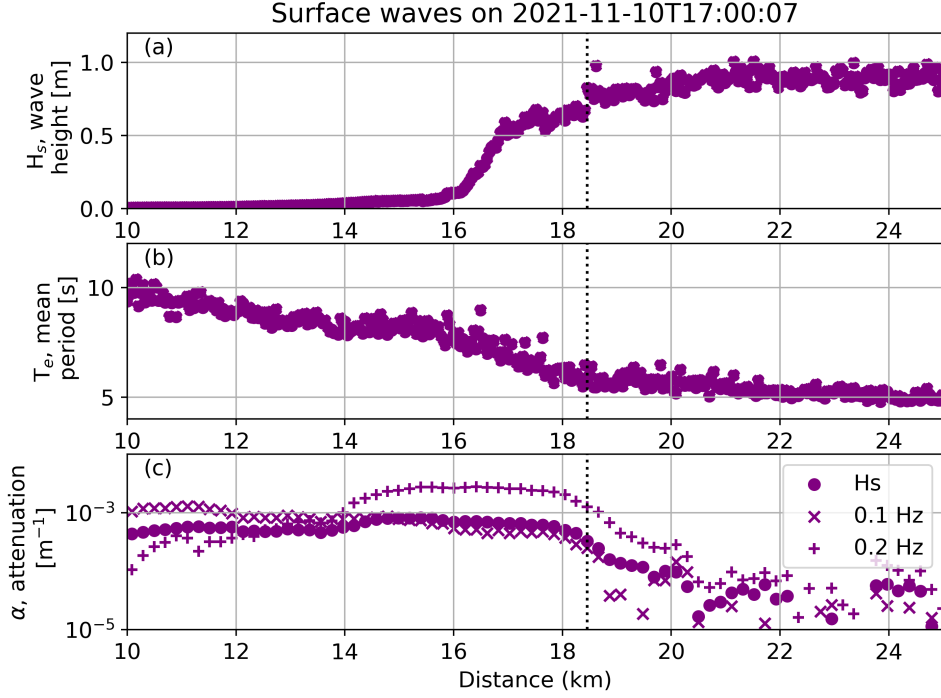


Figure 3. Wave parameters along a cross-section with partial ice cover on November 10, 2021, 17:00. Along-cable estimates of (a) significant wave height, (b) energy-weighted mean wave period, and (c) wave attenuation rates. Wave attenuation is shown for significant wave height (circles), and at 0.1 Hz (x's) and 0.2 Hz (+s), which bracket the range of mean wave periods observed (5–10 s; (c)). The dotted vertical line suggests the inferred location of the ice edge based on a bulk wave height attenuation rate of $3 \times 10^{-4} \text{ m}^{-1}$.

(Squire & Moore, 1980; Waseda et al., 2022). The strongest change is spatially aligned with the steepest change in wave height.

The example cross-section from November 10, 17:00, shows a rapid increase in attenuation rates around 18.5 km, which we expect to be associated with young ice formation (Figure 3c). Attenuation of bulk wave height reaches a maximum of 8.1×10^{-4} approximately 15 km along-cable distance. Attenuation rates are in general higher near the ice edge, and the spectral attenuation at 0.2 Hz reaches a maximum of 2.8×10^{-3} , and remains elevated near this value from approximately 15–18 km. The attenuation values are most similar around 12–14 km distance, where waves have been significantly attenuated and energy has been downshifted to lower frequencies, such that little remains in the higher frequency band. We note that the spectral attenuation at 0.1 Hz becomes greater than that at 0.2 Hz around 14 km, where wave heights are small and little high-frequency wave energy remains. In agreement with prior work (Hošeková et al., 2020), this suggests that the spectral attenuation rates evolve through two-way coupling within heterogeneous wave-ice fields. Constant spectral attenuation rates as a function of ice type or thickness may not be sufficient over large distances. Wave heights are notably small closer to shore (10–14 km), but still show bulk attenuation rates that are characteristic of new frazil and pancake ice ($\sim 5 \times 10^{-4} \text{ m}^{-1}$) (Voermans et al., 2019; Hošeková et al., 2020). Near-zero attenuation rates beyond 20.3 km along-cable distance suggest open water offshore of this location.

For the purposes of subsequent analysis, we use the bulk attenuation to define an “ice edge” at the first incidence of attenuation greater than $3 \times 10^{-4} \text{ m}^{-1}$. For the cross-section shown in Fig. 3, where this “ice edge” is indicated by a vertical dashed line, we can see that there are minor reductions in wave height and period prior to this location that indicate presence of some ice, likely of low concentration and/or very thin. Multiple definitions of the ice edge may be appropriate for different applications.

Mapping bulk wave attenuation as a function of time and space reveals aspects of the spatial evolution of the ice (Figure 4). In general, we suggest that the magnitude of attenuation is correlated primarily with ice concentration and thickness, and the slope of lines in time and space indicate the advection speed of the ice. Using the previously defined “ice edge” cutoff, we map the extent of sea ice as a dashed white line (Fig. 4). The ice edge initially migrates shoreward, with the extent shifting approximately 2.7 km over the 11 hours between November 10 02:00 and 13:00. This corresponds to an approximate velocity of 0.072 m/s. Previous work has suggested that sea ice velocity follows the wave- and wind-driven flow at the surface (Lund et al., 2018). As such, we expect that the translation of the ice edge may be associated with wave-driven Stokes drift. For comparison, we calculate the anticipated Stokes drift \bar{u}_s over this period using the average bulk wave parameters incident on the ice edge:

$$\bar{u}_s = \frac{2g\pi^3 H_s^2}{gT_e^3} \quad (2)$$

giving an approximate velocity of 0.069 m/s at the ice edge. This will of course decay with decreasing H_s and increasing T_e farther into the ice, so it may be insufficient to explain the ice transport.

Another mechanism for ice transport is a gradient in wave radiation stress (i.e., momentum flux), which has been shown to force motion along an ice edge (Thomson, Hošeková, et al., 2021). This mechanism is explicitly related to the wave attenuation rate, because that sets the gradient of the radiation stress (and thus the transfer of momentum from the waves to the ice). For the across ice (shoreward) component and waves normally incident, the expected speed \bar{u} is

$$\bar{u} = H_0 e^{-\alpha x} \sqrt{\frac{\alpha g}{8C_D}}. \quad (3)$$

Using an ice-ocean drag coefficient of $C_D = 8 \times 10^{-3}$ and bulk attenuation of $\alpha = 1 \times 10^{-4}$, this similarly gives an approximate velocity estimate of 0.1 m/s. This shoreward velocity, in addition to the Stokes drift and direct wind drift, likely results in compaction of the ice edge into higher concentration and thicker frazil or pancake layer (e.g., Wadhams, 1983). The compacted ice, in turn, is likely the cause of a local maxima in wave attenuation rate at the ice edge.

From November 10, 13:00, and onwards into November 11, the ice edge nearly uniformly advances offshore. This evolution suggests a combination of offshore ice motion and additional formation of thin, new ice (e.g., 04:00–08:00 on November 11). The ice advance signal is consistent with the results of Baker and Abbott (2022) and Castro et al. (n.d., in review), who used the same dataset to suggest that changes in DAS signal can be used to resolve spatial evolution of ice advance not captured by other methods (e.g., satellite products). After November 11, 08:00, wave signals across the cable approach the lower observable limit, presumably associated with widespread ice advance and reduction of incident waves. ERA5 suggests wind speeds decline from 12 m/s to approximately 7.5 m/s over the period shown in Figure 4.

4 Conclusions

Using a novel surface wave observation method, we observe high spatial variability of wave attenuation rates in new, autumn sea ice. Wave attenuation by thin, new land-

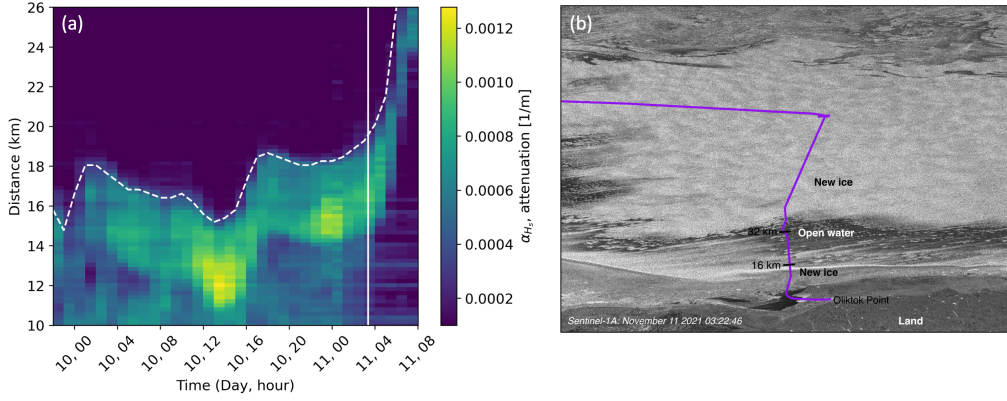


Figure 4. (a) Map of bulk wave height attenuation from November 9, 22:00 - November 11, 08:00, from 10-26 km along-cable distance. Dark blue suggests near-zero attenuation likely associated with open water. Green-yellow corresponding to higher attenuation rates suggest the presence of sea ice, where the dashed white line denotes the approximate ice edge associated with attenuation of greater than $3 \times 10^{-4} \text{ m}^{-1}$. Vertical white line corresponds to time of synthetic aperture radar (SAR) backscatter in (b) from November 11, 03:22, which suggests new ice (lower backscatter; white) to approximately 18 km along-cable distance. Black ticks correspond to 16 and 32 km along-cable distance. Copernicus Sentinel data 2021 retrieved from ASF DAAC May 18 2023, processed by ESA.

fast ice is relatively gradual, leaving open the possibility for incomplete attenuation and coastal impacts during fall storms. The attenuation rates of new, coastal sea ice were similar to those previously observed during autumn evolution off the shelf (Cheng et al., 2017; Hošeková et al., 2020), in the range of $3\text{-}8 \times 10^{-4} \text{ m}^{-1}$. The results here suggest that higher attenuation rates previously observed near the ice-edge may be a result of wave-ice interactions leading to ice compaction and increased thickness. Such high-resolution estimates of wave attenuation will contribute to better understanding the range of wave attenuation coefficients appropriate for different ice types and thicknesses, and implementation in coupled wave-sea ice models.

Seafloor DAS is demonstrated to be a particularly promising method for observing waves in challenging coastal environments, such as the seasonally ice-covered coastal Arctic. We expect this technology to be especially useful during periods of rapid change, including freeze-up (as shown here) and break-out in the spring. Ice break-out is particularly challenging to capture with typical methods due to its episodic nature with rapidly-evolving spatial gradients, and may be well-suited to observation with DAS. Additionally, DAS can provide a non-invasive manner to measure wave exposure of the Arctic coastlines, which is of high utility for understanding rapid erosion rates.

Many unknowns remain in the signal response of seafloor DAS and best practices for retrieval of surface wave parameters. Efforts are currently underway to derive physically-based retrieval methods. Nonetheless, the observations presented here suggest that empirical calibration methods result in realistic wave spectra and bulk wave characteristics that are of use for monitoring and process understanding. We recommend future work using empirical calibration methods for DAS measurements of surface waves to use multiple spatially collocated wave observations covering a range of sea state conditions.

Appendix A Methods

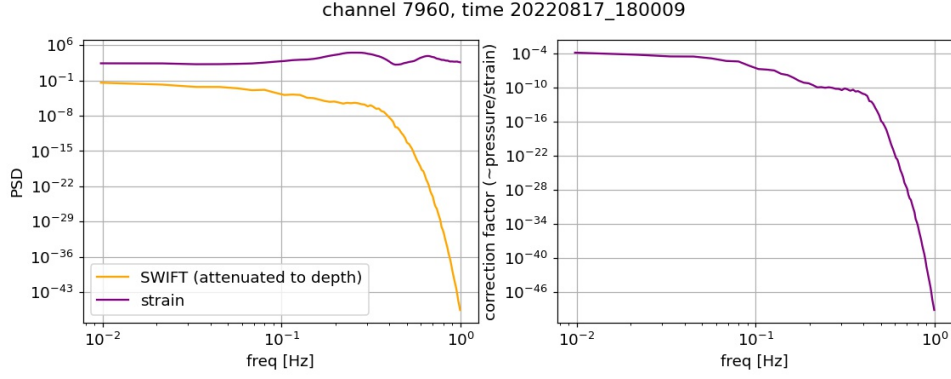


Figure A1. Example calculation of empirical correction factor for channel 7960 (16.2 km along-cable distance) at 18:00 on August 17, 2022. Left panel shows PSD of raw DAS strain-rate (purple) and inferred seafloor pressure from SWIFT (orange). Right panel shows the empirical correction factor calculated as a ratio of the PSDs.

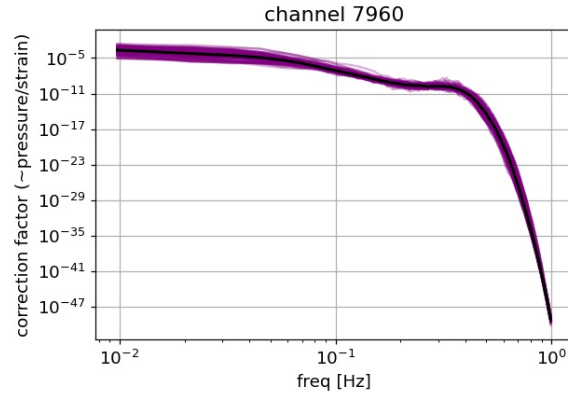


Figure A2. All empirical correction factors for channel 7960 (16.2 km along-cable distance, as in example in Fig. A1). Black line indicates the median value that is used as the channel-specific empirical correction factor in subsequent analysis.

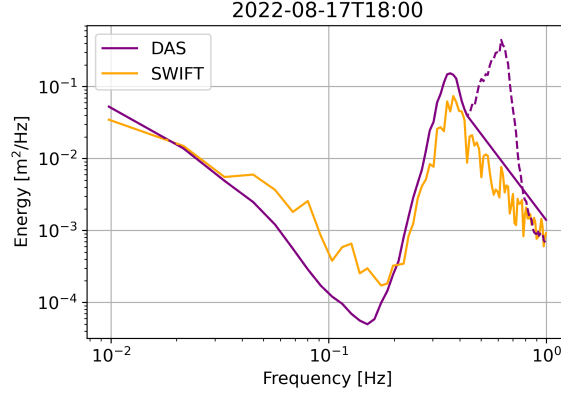


Figure A3. Example of methods for correcting high-frequency noise in wave spectra (see Section 2.4). An inflection point is determined empirically from original DAS-derived spectra (dashed purple line), here around 0.45 Hz. Beyond that, corrected spectra (solid purple line) is fit with the canonical f^{-4} slope for high-frequency waves. Observed wave spectra from SWIFT (orange) shows improved agreement with the corrected spectra. Note that the secondary peak at 0.7 Hz may be evidence of acoustic harmonics from ocean surface gravity waves (e.g., Ardhuin et al., 2013), which will be explored with this dataset in future work.

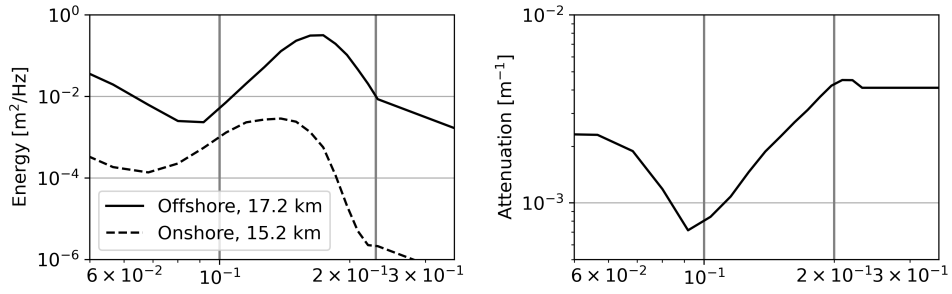


Figure A4. Example calculation of spectral attenuation following Eqn. 1. DAS-derived wave spectra from 17.2 and 15.2 km along-cable distance (left) are used to calculate attenuation rate (right). Vertical lines correspond to the frequency values shown in Figure 3c (×'s and +'s).

Appendix B Open Research

Datasets of derived ocean surface gravity wave parameters have been submitted to the Arctic Data Center for archive. The DAS data recorded by the Cryosphere/Ocean Distributed Acoustic Sensing (CODAS) Experiment for the November 2021 period are archived at Open Energy Data Initiative (mhkdr.openei.org/submissions/438). Code to produce wave DAS-derived wave products is available at github.com/smithmadisonm/DAS-surface-wave-processing. Preliminary data products from the SWIFT wave buoy are available online at <http://faculty.washington.edu/jmt3rd/SWIFTdata/DynamicDataLinks.html>, where the buoy deployed here was SWIFT 18.

Acknowledgments

MS and JT were funded by NSF EAGER grant OPP 2214651. MB and RA were supported by the Laboratory Directed Research and Development program at Sandia Na-

tional Laboratories, a multimission laboratory managed and operated by National Technology and Engineering Solutions of Sandia LLC, a wholly owned subsidiary of Honeywell International Inc. for the U.S. Department of Energy’s National Nuclear Security Administration under contract DE-NA0003525. We thank Quintillion for fiber access and Silixa, LLC, for data collection and analysis advice.

We thank Dr. Emily Eidam and the crew of the R/V Ukpik including Mike Fleming for assistance with deployment of SWIFT buoy. We thank Hannah Glover and Meagan Wengrove for useful discussion on methods for empirical calibration of surface wave measurements from seafloor DAS.

References

- Ardhuin, F., Lavanant, T., Obrebski, M., Marié, L., Royer, J.-Y., d’Eu, J.-F., ... Aucan, J. (2013). A numerical model for ocean ultra-low frequency noise: Wave-generated acoustic-gravity and rayleigh modes. *The Journal of the Acoustical Society of America*, 134(4), 3242–3259.
- Baker, M. G., & Abbott, R. E. (2022). Rapid refreezing of a marginal ice zone across a seafloor distributed acoustic sensor. *Geophysical Research Letters*, e2022GL099880.
- Barnhart, K. R., Overeem, I., & Anderson, R. S. (2014). The effect of changing sea ice on the physical vulnerability of arctic coasts. *The Cryosphere*, 8(5), 1777–1799.
- Bidlot, J.-R. (2012). Present status of wave forecasting at ecmwf. In *Workshop on ocean waves* (pp. 1–17).
- Castro, A. F. P., Schmandt, B., Baker, M. B., & Abbott, R. E. (n.d., in review). Tracking local sea ice extent in the beaufort sea using distributed acoustic sensing and machine learning. *The Seismic Record*.
- Cheng, S., Rogers, W. E., Thomson, J., Smith, M., Doble, M. J., Wadhams, P., ... others (2017). Calibrating a viscoelastic sea ice model for wave propagation in the Arctic fall marginal ice zone. *Journal of Geophysical Research: Oceans*, 122(11), 8770–8793.
- Cohn, N., Bosche, L. V., Midgley, T., Small, C., Douglas, T. A., & King, J. (2022). Assessing drivers of coastal tundra retreat at point hope, alaska. *Journal of Geophysical Research: Earth Surface*, 127(11), e2022JF006813.
- Herbers, T. H. C., Jessen, P. F., Janssen, T. T., Colbert, D. B., & MacMahon, J. H. (2012). Observing ocean surface waves with gps-tracked buoys. *Journal of Atmospheric and Oceanic Technology*, 29, 944–959. doi: <https://doi.org/10.1175/JTECH-D-11-00128.1>
- Hersbach, H., Bell, B., Berrisford, P., Hirahara, S., Horányi, A., Muñoz-Sabater, J., ... others (2020). The era5 global reanalysis. *Quarterly Journal of the Royal Meteorological Society*, 146(730), 1999–2049.
- Hošeková, L., Eidam, E., Panteleev, G., Rainville, L., Rogers, W. E., & Thomson, J. (2021). Landfast ice and coastal wave exposure in northern alaska. *Geophysical Research Letters*, e2021GL095103.
- Hošeková, L., Malila, M. P., Rogers, W. E., Roach, L. A., Eidam, E., Rainville, L., ... Thomson, J. (2020). Attenuation of ocean surface waves in pancake and frazil sea ice along the coast of the chukchi sea. *Journal of Geophysical Research: Oceans*, 125(12), e2020JC016746.
- Kohout, A. L., & Meylan, M. H. (2008). An elastic plate model for wave attenuation and ice floe breaking in the marginal ice zone. *Journal of Geophysical Research: Oceans*, 113(C9), n/a–n/a. Retrieved from <http://dx.doi.org/10.1029/2007JC004434> doi: 10.1029/2007JC004434
- Kohout, A. L., Smith, M., Roach, L. A., Williams, G., Montiel, F., & Williams, M. J. (2020). Observations of exponential wave attenuation in antarctic sea ice

- during the pipers campaign. *Annals of Glaciology*, 61(82), 196–209.
- Landrø, M., Bouffaut, L., Kriesell, H. J., Potter, J. R., Rørstadbotnen, R. A., Taweessintanon, K., ... others (2022). Sensing whales, storms, ships and earthquakes using an arctic fibre optic cable. *Scientific Reports*, 12(1), 19226.
- Lindsey, N. J., Dawe, T. C., & Ajo-Franklin, J. B. (2019). Illuminating seafloor faults and ocean dynamics with dark fiber distributed acoustic sensing. *Science*, 366(6469), 1103–1107.
- Liu, P. C. (1989). On the slope of the equilibrium range in the frequency spectrum of wind waves. *Journal of Geophysical Research: Oceans*, 94(C4), 5017–5023.
- Lund, B., Graber, H. C., Smith, M., Doble, M., Persson, O., Thomson, J., & Wadhams, P. (2018). Arctic sea ice drift measured by shipboard marine radar. *Journal of Geophysical Research: Oceans*, 123(6). doi: 10.1029/2018JC013769
- Mahoney, A. (2018). Landfast sea ice in a changing arctic. *Arctic Report Card 2018*, 99.
- Mahoney, A., Eicken, H., Gaylord, A. G., & Gens, R. (2014). Landfast sea ice extent in the chukchi and beaufort seas: The annual cycle and decadal variability. *Cold Regions Science and Technology*, 103, 41–56.
- Meylan, M. H., Bennetts, L. G., Mosig, J., Rogers, W., Doble, M., & Peter, M. A. (2018). Dispersion relations, power laws, and energy loss for waves in the marginal ice zone. *Journal of Geophysical Research: Oceans*, 123(5), 3322–3335.
- Rogers, W. E., Meylan, M. H., & Kohout, A. L. (2021). Estimates of spectral wave attenuation in antarctic sea ice, using model/data inversion. *Cold Regions Science and Technology*, 182, 103198.
- Sidenko, E., Tertyshnikov, K., Lebedev, M., & Pevzner, R. (2022). Experimental study of temperature change effect on distributed acoustic sensing continuous measurements. *Geophysics*, 87(3), D111–D122.
- Squire, V. A. (2019). Ocean wave interactions with sea ice: A 2019 reappraisal. *Annu. Rev. Fluid Mech.*, 44, 1–25.
- Squire, V. A., & Moore, S. C. (1980). Direct measurement of the attenuation of ocean waves by pack ice. *Nature*, 283, 365–368.
- Thomson, J. (2012). Wave breaking dissipation observed with "SWIFT" drifters. *Journal of Atmospheric and Oceanic Technology*, 29, 1866–1882. doi: 10.1175/JTECH-D-12-00018.1
- Thomson, J. (2022). Wave propagation in the marginal ice zone: connections and feedback mechanisms within the air–ice–ocean system. *Philosophical Transactions of the Royal Society A*, 380(2235), 20210251.
- Thomson, J., Eidam, E., Hosekova, L., de Klerk, A., Roth, E., Roberts, S., & Naber, D. (2020). *Coda cruise report, r/v sikuliaq, sept-oct 2020* (Tech. Rep.). https://www.apl.washington.edu/project/projects/coda/pdfs/cruise_report_2020.pdf.
- Thomson, J., Garton, J. B., Jha, R., & Trapani, A. (2018). Measurements of directional wave spectra and wind stress from a wave glider autonomous surface vehicle. *Journal of Atmospheric and Oceanic Technology*, 35(2), 347–363.
- Thomson, J., Hošeková, L., Meylan, M. H., Kohout, A. L., & Kumar, N. (2021). Spurious rollover of wave attenuation rates in sea ice caused by noise in field measurements. *Journal of Geophysical Research: Oceans*, 126(3), e2020JC016606.
- Thomson, J., Lund, B., Hargrove, J., Smith, M. M., Horstmann, J., & MacKinnon, J. A. (2021). Wave-driven flow along a compact marginal ice zone. *Geophysical Research Letters*, 48(3), e2020GL090735.
- Thomson, J., & Rogers, W. E. (2014). Swell and sea in the emerging arctic ocean. *Geophysical Research Letters*, 41(9), 3136–3140. doi: 10.1002/2014GL059983
- Voermans, J. J., Babanin, A. V., Thomson, J., Smith, M. M., & Shen, H. H. (2019). Wave attenuation by sea ice turbulence. *Geophysical Research Letters*.

- 446 Wadhams, P. (1983). A mechanism for the formation of ice edge bands. *Journal of*
447 *Geophysical Research: Oceans*, 88(C5), 2813–2818.
- 448 Waseda, T., Alberello, A., Nose, T., Toyota, T., Kodaira, T., & Fujiwara, Y. (2022).
449 Observation of anomalous spectral downshifting of waves in the okhotsk
450 sea marginal ice zone. *Philosophical Transactions of the Royal Society A*,
451 380(2235), 20210256.
- 452 Wilcock, W. S., Abadi, S., & Lipovsky, B. P. (2023). Distributed acoustic sensing
453 recordings of low-frequency whale calls and ship noise offshore central oregon.
454 *JASA Express Letters*, 3(2), 026002.
- 455 Williams, E. F., Fernández-Ruiz, M. R., Magalhaes, R., Vanthillo, R., Zhan, Z.,
456 González-Herráez, M., & Martins, H. F. (2019). Distributed sensing of mi-
457 croseisms and teleseisms with submarine dark fibers. *Nature communications*,
458 10(1), 1–11.